

CUT FINITE ELEMENT DISCRETIZATIONS OF CELL-BY-CELL EMI ELECTROPHYSIOLOGY MODELS*

NANNA BERRE[†], MARIE E. ROGNES[‡], AND ANDRÉ MASSING[§]

Abstract. The EMI (Extracellular-Membrane-Intracellular) model describes electrical activity in excitable tissue, where the extracellular and intracellular spaces and cellular membrane are explicitly represented. The model couples a system of partial differential equations in the intracellular and extracellular spaces with a system of ordinary differential equations on the membrane. A key challenge for the EMI model is the generation of high-quality meshes conforming to the complex geometries of brain cells. To overcome this challenge, we propose a novel cut finite element method (CutFEM) where the membrane geometry can be represented independently of a structured and easy-to-generated background mesh for the remaining computational domain.

Starting from a Godunov splitting scheme, the EMI model is split into separate PDE and ODE parts. The resulting PDE part is a non-standard elliptic interface problem, for which we devise two different CutFEM formulations: one single-dimensional formulation with the intra/extracellular electrical potentials as unknowns, and a multi-dimensional formulation that also introduces the electrical current over the membrane as an additional unknown leading to a penalized saddle point problem. Both formulations are augmented by suitably designed ghost penalties to ensure stability and convergence properties that are insensitive to how the membrane surface mesh cuts the background mesh. For the ODE part, we introduce a new unfitted discretization to solve the membrane bound ODEs on a membrane interface that is not aligned with the background mesh. Finally, we perform extensive numerical experiments to demonstrate that CutFEM is a promising approach to efficiently simulate electrical activity in geometrically resolved brain cells.

Key words. cut finite elements, electrophysiology, coupled ODE-PDEs, neuroscience

AMS subject classifications. 65M60, 65M85, 65N30, 65N85, 92C20

1. Introduction. Today, classical paradigms for modelling electrophysiology such as the bidomain model [50] are being challenged by new mathematical frameworks that explicitly represent and resolve the geometry of extracellular and intracellular spaces [1, 51, 43, 23, 49, 31, 22]. This evolution is jointly driven by impressive advances in medical physics and technology, allowing for in-vivo imaging of intracellular and extracellular dynamics as well as microscopy at the subcellular level, and by advances in computational resources, making the previously uncomputable computable. These cell-based frameworks, referred to as *extracellular-membrane-intracellular* (EMI) models [51] or *cell-by-cell electrophysiology* models [22] or *electrophysiology with internal boundaries* [43], take the form of coupled systems of ordinary and partial differential equations (ODEs, PDEs). Typically, the PDEs are defined relative to disjoint domains of dimension d coupled over a topologically $d - 1$ -dimensional internal interface, while the ODEs are defined over the lower-dimensional manifold alone. These types of equations frequently appear in electrophysiology: to model the electrical activity of heart cells with polarized membrane features [31] or that in neurons, extracellular space and glial cells [1, 23], while the PDE subproblems are also frequently encountered in chemical and electrical engineering such as for modelling

*Submitted to pre-print server and journal (July 6, 2023).

Funding: M. E. Rognes graciously acknowledges support and funding from the Research Council of Norway (RCN) via FRIPRO grant agreement #324239 (EMIX)

[†]Department of Mathematical Sciences, Norwegian University of Science and Technology, Trondheim, Norway (nanna.berre@ntnu.no)

[‡]Department for Numerical Analysis and Scientific Computing, Simula Research Laboratory, Oslo, Norway (meg@simula.no)

[§]Department of Mathematical Sciences, Norwegian University of Science and Technology, Trondheim, Norway (andre.massing@ntnu.no)

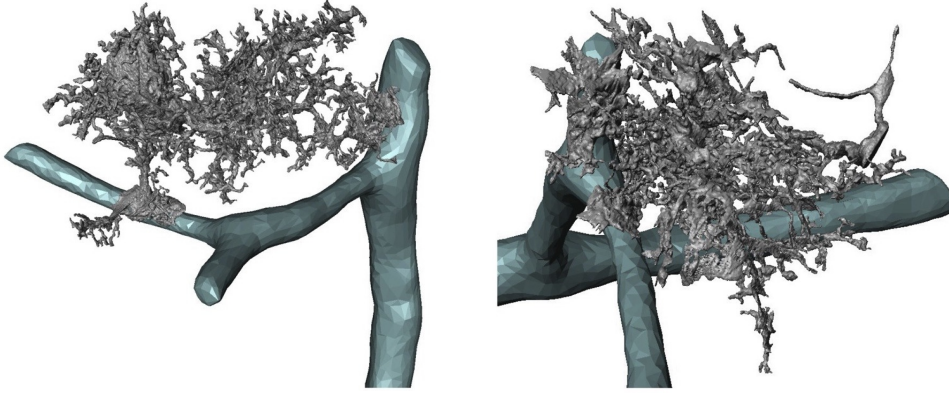


Fig. 1.1: Example of 3d reconstruction of astrocytes morphology from [19], adapted(cropped) under the Creative Commons CC-BY license.

thermal contact resistance [7].

In all of these cases, the geometry is chiefly defined by the lower-dimensional surface, e.g. the cell membranes or composite media interfaces, frequently in the form of an image-derived STL surface. The associated cellular domains may be non-convex, narrow and tortuous, placing high demands on the resolution required for conforming volumetric meshes and essentially forcing the numerical resolution to be dictated by geometrical rather than approximation considerations. Moreover, without suitable post-processing, the quality of the generated STL surface meshes might be insufficient to generate high-quality 3D unstructured volume meshes required for accurate finite element-based computations.

A natural alternative is to instead consider unfitted meshes and discretizations such as cut finite element methods (CutFEM) [13], finite cell methods (FCM) [46], shifted boundary method (SBM) [3], aggregated unfitted finite element methods (AgFEM) [5], as well as unfitted discontinuous Galerkin methods [6, 28] and methods based on immersogeometric analysis [47], see [21] for a recent state-of-the-art review. A key advantage of the unfitted finite element technology is that allows to embed the image-derived, and potentially lower quality, surface mesh into an easy-to-generate structured background mesh in a non-conforming manner without scarifying the approximation power of the underlying finite element spaces. As a result, the costly generation of high-resolution and high-quality unstructured 3D volume meshes for finite element based computations is completely circumvented, potentially leading to more streamlined and semi-automated simulation pipelines. Such image-based finite element analyses of biological media has been successfully used in [48, 55, 20], to predict the elastic responses of bone structures. However, the use of image-based models is barely explored in the computational neuroscience community, and only very recently, unfitted finite element methods have been employed to simulate astrocytic metabolism in realistic three-dimensional geometries [26, 25], as well to solve the electroencephalography (EEG) forward problem [45, 24].

1.1. New contributions and outline of the paper. In all the aforementioned contributions, unfitted finite element methods were devised to solve elliptic and parabolic problems with boundary conditions posed on imaged-derived surfaces meshes.

The computational modeling of electric activity in geometrically resolved excitable cells on the other hand requires to consider *multi-dimensional* surface-bulk problems which couples an elliptic interface PDE defined on the extra/intracellular bulk domains with a nonlinear system of ODEs solely posed on the membrane surface. In the present work, we introduce two cut finite element methods for the robust and accurate discretization of such multi-dimensional EMI systems. Our method departs from an earlier developed Godunov splitting scheme for the model [51], which decouples the PDE part from the ODE part. For the PDE step, different weak formulations can be derived [36] and we propose CutFEM-based discretizations for two of them. First, we consider a single-dimensional formulation with the intra/extracellular electrical potentials as unknowns. This approach is inspired by [33] who analyzed and successfully applied such a discretization for approximating the temperature in composite media with contact resistance. In the second, multi-dimensional formulation, the electrical current over the membrane is introduced as an additional unknown which formally results in a generalized saddle point problem with a penalty-like term. By augmenting the considered weak formulations with suitably designed, so-called ghost penalties [13], we ensure that the resulting discretizations are geometrically robust so that their stability and accuracy is not affected by how the membrane surface mesh and the structured background mesh intersect.

In addition to the proposed CutFEM-based discretizations of elliptic problem with a contact resistance interface condition, we also introduce a CutFEM formulation of the ODE system posed on the unfitted membrane surface. In contrast to fitting approaches, solving the ODE system directly in the surface mesh nodes makes it challenging from an implementation point of view to interface with the PDE problem. Moreover, the STL mesh can be of low quality with potentially large variations in both the size and the aspect ratio of the individual triangles. Our approach borrows ideas from the CutFEM discretization of surface PDEs [16] and allows for an easy and seamless integration of the ODE and PDE step. Solvers and simulation code for the present work are based on Julia [9] and the finite element framework Gridap [4], and is openly available [8]. In summary, the main contributions of this paper are as follows.

- We introduce a complete unfitted discretization approach for the EMI/cell-by-cell electrophysiology equations and demonstrate its robustness and applicability on idealized and image-based geometries.
- We propose different CutFEM discretization techniques for the Poisson interface problem, both single-dimensional and multi-dimensional formulations and provide detailed numerical evidence of their well-posedness, approximation properties, and geometrical robustness.
- We introduce an unfitted discretization technique for systems of nonlinear, spatially-dependent ODEs defined over the interface in the absence of a conforming interface representation.

This paper is structured as follows. We describe the cell-by-cell electrophysiology (EMI) model in Section 2, and outline a classical operator splitting algorithm separating this system of time-dependent, nonlinear, coupled equations into a set of ODEs and a set of PDEs in the brief Section 3. In Section 4, we introduce two unfitted (CutFEM) formulations of the PDEs: a single-dimensional formulation for the intra-cellular and extracellular potential alone, and a multi-dimensional formulation for the intracellular and extracellular potentials as well as the membrane flux. We prove that both formulations are well-posed and discuss unfitted stabilization operators. We turn to the system of ODEs in Section 5 and introduce a discretization technique for such system of equations living on an interface, but without an explicit discrete represen-

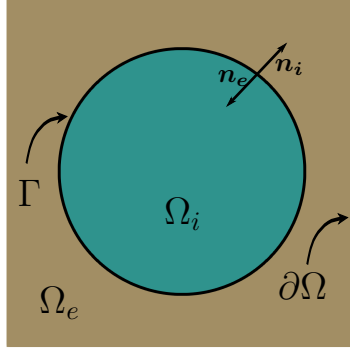


Fig. 2.1: Illustration of the domains in the EMI model.

tation of the interface. We study the approximation and solvability properties of the ODE-, PDE- and coupled discretizations in [Section 6](#), before concluding in [Section 7](#).

2. The cell-by-cell EMI electrophysiology model. The EMI model [[1](#), [51](#), [32](#), [22](#)] is a multi-dimensional multi-physics problem that couples a linear Poisson-interface problem in the intra- and extracellular domains to a system of nonlinear ODEs on the membrane interface. More precisely, assume that the complete computational domain Ω is separated into an extracellular domain Ω_e and an intracellular domain Ω_i with $\partial\Omega_i \cap \partial\Omega_e = \emptyset$, and such that Ω_i is strictly contained in Ω . The membrane of the cell is defined as the intersection of the closures of Ω_e and Ω_i and is denoted by Γ ([Figure 2.1](#)). The EMI model describes the spatial-temporal extracellular potential u_e , intracellular potential u_i , and the transmembrane potential v governed by the following equations:

$$\begin{aligned}
 (2.1a) \quad & -\nabla \cdot (\sigma_e \nabla u_e) = 0 && \text{in } \Omega_e, \\
 (2.1b) \quad & -\nabla \cdot (\sigma_i \nabla u_i) = 0 && \text{in } \Omega_i, \\
 (2.1c) \quad & \sigma_e \nabla u_e \cdot \mathbf{n}_e = -\sigma_i \nabla u_i \cdot \mathbf{n}_i \equiv I_m && \text{on } \Gamma, \\
 (2.1d) \quad & v = u_i - u_e && \text{on } \Gamma, \\
 (2.1e) \quad & C_m \partial_t v = I_m - I_{\text{ion}}(v, s) && \text{on } \Gamma, \\
 (2.1f) \quad & \partial_t s = F(s, v) && \text{on } \Gamma,
 \end{aligned}$$

where the intracellular and extracellular conductivities are denoted by σ_i and σ_e , and C_m is the membrane capacitance. Next, the ionic current density is given by I_{ion} and the total membrane current density by I_m . Finally, \mathbf{n}_i denotes the normal pointing out from Ω_i , and $\mathbf{n}_e = -\mathbf{n}_i$.

The ionic current density I_{ion} governs the membrane potential and is subject to further modeling. In this work, the Hodgkin-Huxley model [[29](#)] will be used, where I_{ion} is given as follows

$$(2.2) \quad I_{\text{ion}} = \bar{g}_{Na} m^3 h (v - E_{Na}) + \bar{g}_K n^4 (v - E_K) + \bar{g}_L (v - E_L) - I_{\text{app}},$$

with \bar{g}_{Na} , \bar{g}_K and \bar{g}_L being the maximal conductivities related to sodium, potassium and a leak channel, respectively. The gating variables m and h are used to model the probability of gates being open to the passage of sodium ions, and the corresponding gating variable for potassium is denoted by n . Equilibrium potentials, which indicate

Table 1: Parameter values for the Hodgkin-Huxley model

Parameter	Symbol	Value	Unit	Reference
Membrane capacitance	C_m	$2 \cdot 10^{-5}$	$\frac{\text{nF}}{\mu\text{m}^2}$	[52]
Na+ HH max conductivity	\bar{g}_{Na}	$1.2 \cdot 10^{-3}$	$\frac{\mu\text{S}}{\mu\text{m}^2}$	[29]
K+ HH max conductivity	\bar{g}_K	$3.6 \cdot 10^{-4}$	$\frac{\mu\text{S}}{\mu\text{m}^2}$	[29]
Stimulus	g_{stim}	$7 \cdot 10^{-3}$	$\frac{\mu\text{S}}{\mu\text{m}^2}$	
Leak conductivity	\bar{g}_L	$3 \cdot 10^{-6}$	$\frac{\mu\text{S}}{\mu\text{m}^2}$	[29]
Na+ equilibrium potential	E_{Na}	50	mV	[29]
K+ equilibrium potential	E_K	-77	mV	[29]
Leak equilibrium potential	E_L	-54.5	mV	[29]
Initial membrane potential	v^0	-67.7	mV	
Resting membrane potential	v_{rest}	-65	mV	
Intracellular conductivity	σ_i	0.7	$\frac{\mu\text{S}}{\mu\text{m}}$	[52]
Extracellular conductivity	σ_e	0.3	$\frac{\mu\text{S}}{\mu\text{m}}$	[52]
Initial HH gating value (Na+)	m^0	0.0379		[29]
Initial HH gating value (Na+)	h^0	0.688		[29]
Initial HH gating value (K+)	n^0	0.276		[29]

at which potentials sodium, potassium, and the leak channel are in equilibrium, are denoted by E_{Na} , E_K , and E_L , respectively. Importantly, these gating variables are modeled with the following ODEs

$$(2.3) \quad p_t = \alpha_p(v)(1 - p) - \beta_p(v)p,$$

for $p \in \{m, h, n\}$, where the following expressions are used for α and β [29],

$$\begin{aligned} \alpha_m &= 0.1 \frac{25 - v_M}{\exp((25 - v_M)/10) - 1}, & \beta_m &= 4 \exp(-v_M/18), \\ \alpha_h &= 0.07 \exp(-v_M/20), & \beta_h &= \frac{1}{\exp((30 - v_M)/10) + 1}, \\ \alpha_n &= 0.01 \frac{10 - v_M}{\exp((10 - v_M)/10) - 1}, & \beta_n &= 0.125 \exp(-v_M/80). \end{aligned}$$

Here $v_M = v - v_{\text{rest}}$ with v_{rest} being the resting potential. Parameter values for the Hodgkin-Huxley model are listed in Table 1.

In addition, we impose an applied stimulus I_{app}

$$I_{\text{app}} = g_{\text{stim}} H(x) T(t)$$

where

$$H(x) = \begin{cases} 1 & \text{if } \mathbf{x} \in D, \\ 0 & \text{else,} \end{cases} \quad T(t) = \begin{cases} 1 & \text{if } t \in [t_1, t_2], \\ 0 & \text{else,} \end{cases}$$

are the indicator functions of some domain $D \subset \Omega$ and some time interval $[t_1, t_2]$.

3. Operator splitting and time discretization of the EMI model. The EMI model with Hodgkin-Huxley membrane dynamics consists of a PDE system coupled with an ODE system. We employ a standard operator splitting scheme to decouple the problem into smaller subproblems. Each subproblem can then be solved with solution methods dedicated to the specific subproblem. A classical approach is Godunov splitting [39], which has previously successfully been applied to the EMI model [51, 30], to decouple the membrane-confined ODE system from the PDE system.

To discretize the PDE step in time we apply an implicit Euler discretization and denote the size of the time step by Δt . For the ODE system, we discretize pointwise in time, using an explicit Euler step to pass from t^m to $t^{m+1} = t^m + \Delta t$. The time-discretized splitting scheme is given in Algorithm 3.1.

Algorithm 3.1 Time-discretized splitting scheme for the EMI model

Given initial values v^0, s^0

for timestep $m = 1 : M$ **do**

(ODE-step) Compute v^*, s^m by solving

$$(3.1a) \quad v^*(x) - v^{m-1}(x) = -\Delta t I_{\text{ion}}(v^{m-1}(x), s^{m-1}(x)),$$

$$(3.1b) \quad s^{m+1}(x) - s^{m-1}(x) = \Delta t F(v^{m-1}(x), s^{m-1}(x)).$$

(PDE-step) Compute u_i^m, u_e^m, v^m by solving

$$(3.2a) \quad -\nabla \cdot (\sigma_e \nabla u_e^m) = 0 \quad \text{in } \Omega_e,$$

$$(3.2b) \quad -\nabla \cdot (\sigma_i \nabla u_i^m) = 0 \quad \text{in } \Omega_i,$$

$$(3.2c) \quad \sigma_e \nabla u_e^m \cdot \mathbf{n}_e = -\sigma_i \nabla u_i^m \cdot \mathbf{n}_i \equiv I_m^m \quad \text{on } \Gamma,$$

$$(3.2d) \quad u_i^m - u_e^m = C_m^{-1} \Delta t I_m^m + g \quad \text{on } \Gamma,$$

$$(3.2e) \quad u_e^m = 0 \quad \text{on } \partial\Omega,$$

 where $g = v^*$.

end for

return u_e, u_i and v .

4. Unfitted discretizations of the EMI PDE step. The main focus of the remainder of this paper is discretizing the PDE system (3.2) of the PDE-step in Algorithm 3.1. This system takes the form of two Poisson problems coupled by a Robin-type interface condition, for which several finite element methods have been proposed. Belgacem et al. [7] modelled contact resistance problems via systems with the same structure, presenting two different formulations. The first uses only the potentials as unknowns, while the second is a hybrid dual formulation introducing also the current densities. Using the nomenclature introduced by Kuchta et al. [36], we will refer to the first one as the single-dimensional primal formulation. Two other alternatives were presented in by Tveito et al. [51], a multi-dimensional primal formulation with the potentials and the current across the membrane as unknowns, and a multi-dimensional mixed formulation where in addition also the current densities were unknowns. An unfitted method based on the single-dimensional primal formulation was presented by Ji et al. [33]. We first review this formulation, before presenting a cut finite element formulation based on the multi-dimensional primal formulation.

4.1. A single-dimensional primal formulation of the EMI PDEs. Following the presentation in [36], a weak formulation of (3.2) can be derived as follows. Define the function spaces

$$V_i = H^1(\Omega_i), \quad V_e = H_{0,\partial\Omega}^1(\Omega_e),$$

where the vanishing boundary-trace space is given by

$$(4.1) \quad H_{0,\partial\Omega}^1(\Omega_e) = \{v_e \in H^1(\Omega_e) \mid \text{tr } v_e = 0 \text{ on } \partial\Omega\},$$

and let $V = V_i \times V_e$. We multiply (3.2b) by a test function $v_i \in V_i$ and integrate over Ω_i , and multiply (3.2a) with a test function $v_e \in V_e$ and integrate over Ω_e . Integration by parts then gives

$$(4.2a) \quad \int_{\Omega_e} \sigma_e \nabla u_e \cdot \nabla v_e \, dx - \int_{\Gamma} \sigma_e \nabla u_e \cdot \mathbf{n}_e v_e \, ds = 0,$$

$$(4.2b) \quad \int_{\Omega_i} \sigma_i \nabla u_i \cdot \nabla v_i \, dx - \int_{\Gamma} \sigma_i \nabla u_i \cdot \mathbf{n}_i v_i \, ds = 0.$$

Inserting (3.2c) and (3.2d) into (4.2) gives the abstract problem: find $u \in V$ such that

$$(4.3) \quad a(u, v) = l(v) \quad \forall v \in V,$$

where the bilinear form $a(\cdot, \cdot)$ and the linear form $l(\cdot)$ are given by

$$(4.4) \quad a(u, v) = \int_{\Omega_e} \sigma_i \nabla u_i \cdot \nabla v_i \, dx + \int_{\Omega_i} \sigma_e \nabla u_e \cdot \nabla v_e \, dx + \frac{C_m}{\Delta t} \int_{\Gamma} (u_e - u_i)(v_e - v_i) \, ds,$$

$$(4.5) \quad l(v) = \frac{C_m}{\Delta t} \int_{\Gamma} g(v_i - v_e) \, ds.$$

The bilinear form (4.4) induces the following natural energy norm for $v = (v_i, v_e) \in V = V_i \times V_e$,

$$(4.6) \quad \|v\|_a^2 := \sigma_e \|\nabla v_e\|_{L^2(\Omega_e)}^2 + \sigma_i \|\nabla v_i\|_{L^2(\Omega_i)}^2 + \frac{C_m}{\Delta t} \|v_e - v_i\|_{\Gamma}^2.$$

The weak formulation is clearly coercive and bounded with respect to $\|\cdot\|_a$, and therefore the formulation (4.3) is well-posed thanks to the Lax-Milgram theorem.

4.1.1. Cut finite element formulation. We discretize the formulation (4.3) using a cut finite element method (CutFEM) [13] approach to allow for a more flexible handling of the membrane interface geometry. We start from a structured background mesh $\tilde{\mathcal{T}}_h$ consisting of either n -simplices or n -cubes which cover $\bar{\Omega}$ (see Figure 4.1). Then the active background mesh associated with each of the two subdomains is given by the collections of elements which intersect the corresponding physical domain,

$$(4.7) \quad \mathcal{T}_{h,j} = \{T \in \tilde{\mathcal{T}}_h \mid T \cap \overset{\circ}{\Omega}_j \neq \emptyset\}, \quad j \in \{i, e\},$$

where $\overset{\circ}{\Omega}_i = \Omega_i \setminus \Gamma$, and $\overset{\circ}{\Omega}_e = \Omega_e \setminus (\Gamma \cup \partial\Omega)$. The sets of interior faces are denoted by

$$(4.8) \quad \mathcal{F}_{h,i} = \{F = T^+ \cap T^- \mid T^+, T^- \in \mathcal{T}_{h,i} \text{ and } T^+ \neq T^-\}.$$

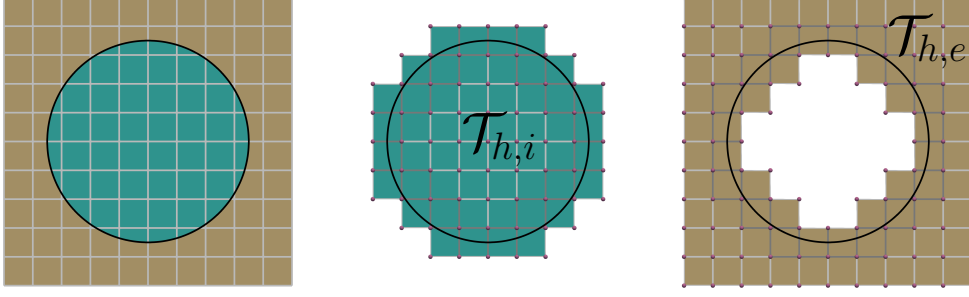


Fig. 4.1: Illustration of the total computational domain(left) the single-dimensional discretization and the (left) intracellular and (right) extracellular computational domains, with corresponding ghost facets.

Also, the set of ghost penalty faces \mathcal{F}_h^g , is given by the set of interior faces in the active mesh belonging to elements that are intersected by the boundary Γ ,

$$(4.9) \quad \mathcal{F}_{h,i}^g = \{F \in \mathcal{F}_{h,i} : T^+ \cap \Gamma \neq \emptyset \vee T^- \cap \Gamma \neq \emptyset\}.$$

Let the jump across an interior face $F \in \mathcal{F}_h$ be

$$(4.10) \quad [w]|_F = w_F^+ - w_F^-,$$

where $w^\pm(x) = \lim_{t \rightarrow 0^+} w(x \mp t \mathbf{n}_F)$ for some chosen unit face normal \mathbf{n}_F .

On a given mesh \mathcal{T}_h , the corresponding space of piecewise continuous polynomials of degree k is denoted by

$$(4.11) \quad \mathbb{P}_c^k(\mathcal{T}_h) = \{v \in C(\Omega_h) : v|_T \in \mathbb{P}^k(T) \ \forall T \in \mathcal{T}_h\},$$

where $\Omega_h = \bigcup_{T \in \mathcal{T}_h} T$, and $\mathbb{P}^k(T)$ is the set for all (multivariate if applicable) polynomials with degree smaller than or equal to k on T . As discretization of the function space V_i and V_e , we define the finite element spaces

$$(4.12) \quad V_{h,i} = \mathbb{P}_c^k(\mathcal{T}_{h,i}), \quad V_{h,e} = \{v \in \mathbb{P}_c^k(\mathcal{T}_{h,e}) \mid v|_{\partial\Omega} = 0\},$$

and the resulting total finite element space $V_h = V_{h,i} \times V_{h,e}$.

Since $V_h \subset V$, the Lax-Milgram theorem again ensures that the resulting discrete problem where we seek $u_h = (u_{h,i}, u_{h,e}) \in V_h$ such that

$$(4.13) \quad a(u_h, v) = l(v) \quad \forall v \in V_h$$

is well-posed. Furthermore, optimal convergence estimates can be derived [33], even without any CutFEM related addition stabilization [40], despite using an unfitted finite element approach. The main reason is that the interface conditions are included naturally and thus leaves the bilinear form unchanged in the discrete formulation, so that the coercivity properties are automatically inherited from continuous weak formulation (4.3). This is in contrast to problems where the weak form needs to be altered because of the imposition of essential boundary or interface conditions, see e.g. the discussion in [13, 28].

However, without any stabilization or further intervention, the possible presence of so-called small cut elements $T \cap \Omega_j$ where $|T \cap \Omega_j| \ll |T|$ can lead to a nearly

singular system matrix and consequently excessively high condition numbers, which in turn can dramatically limit the use and development of efficient iterative solvers. To render the discretization scheme truly geometrical robust, we want to ensure that the resulting condition numbers only depends as usual on the size of the linear system but not on the relative positioning of the membrane interface within the background mesh. We therefore add to (4.13) the following ghost penalty [15, 42, 28],

$$(4.14) \quad g_h(v, w) = g_{h,i}(v_i, w_i) + g_{h,e}(v_e, w_e),$$

where

$$(4.15) \quad g_{h,j}(v_j, w_j) = \sum_{m=0}^k \gamma_m h^{2m+1} ([\partial_n^m v_j], [\partial_n^m w_j])_{\mathcal{F}_{h,j}^g}.$$

The h -scaling of the ghost penalty employed here is chosen such that the physical L^2 -norm augmented with the semi-norm induced by the ghost penalty is equivalent to the L^2 -norm on the corresponding active mesh,

$$\|v_{h,j}\|_{\mathcal{T}_{h,j}}^2 \sim \|v_{h,j}\|_{\Omega_j}^2 + |v_{h,j}|_{g_{h,j}}^2 \quad \forall v_{h,j} \in V_{h,j}, \quad j \in \{i, e\},$$

see, e.g. [28] for a detailed discussion.

The final stabilized CutFEM single-dimensional formulation is then: find $u_h = (u_{h,i}, u_{h,e}) \in V_h$ such that

$$(4.16) \quad A_h(u_h, v) \equiv a(u_h, v) + g_h(u_h, v) = l(v),$$

for all $v = (v_i, v_e) \in V_h$. This formulation converges at optimal rates in the H^1 - and L^2 -norms, and the corresponding condition number is bounded by $\mathcal{O}(h^{-2})$ [33].

4.2. A multi-dimensional weak formulation. Next, we discuss how the EMI PDEs (3.2) can be cast into a penalized saddle point problem using the multi-dimensional primal formulation presented in [36]. As for the single-dimensional formulation, we start from the function spaces

$$(4.17) \quad V_i := H^1(\Omega_i), \quad V_e = H_0^1(\Omega_e), \quad V = V_i \times V_e.$$

Next, we multiply (3.2a) and (3.2b) with test functions from V_e and V_i and use integration by parts to obtain

$$(4.18) \quad \int_{\Omega_e} \sigma_e \nabla u_e \cdot \nabla v_e \, dx - \int_{\Gamma} v_e I_m \, ds = 0,$$

$$(4.19) \quad \int_{\Omega_i} \sigma_i \nabla u_i \cdot \nabla v_i \, dx + \int_{\Gamma} v_i I_m \, ds = 0.$$

In contrast to the single-dimensional formulation, we now leave I_m as a separate unknown. Define the additional function spaces

$$(4.20) \quad Q = H^{-\frac{1}{2}}(\Gamma), \quad Q_c = L^2(\Gamma),$$

and let $I_m \in Q_c$. Multiply (3.2d) by $j_m \in Q_c$ to obtain the last equation,

$$(4.21) \quad \int_{\Gamma} (u_i - u_e) j_m \, ds - \frac{\Delta t}{C_m} \int_{\Gamma} I_m j_m \, ds = \int_{\Gamma} g j_m \, ds.$$

Note that the main reason for choosing the subspace $Q_c \subset Q$ as function space for I_m, j_m is to make sense of the second term appearing in the left-hand side of (4.21).

The resulting multi-dimensional primal formulation is then: find $u_i \in V_i$, $u_e \in V_e$, $I_m \in Q_c$ such that

$$(4.22a) \quad \int_{\Omega_e} \sigma_e \nabla u_e \cdot \nabla v_e \, dx - \int_{\Gamma} v_e I_m \, ds = 0,$$

$$(4.22b) \quad \int_{\Omega_i} \sigma_i \nabla u_i \cdot \nabla v_i \, dx + \int_{\Gamma} v_i I_m \, ds = 0,$$

$$(4.22c) \quad \int_{\Gamma} (u_i - u_e) j_m \, ds - \frac{\Delta t}{C_m} \int_{\Gamma} I_m j_m \, ds = \int_{\Gamma} g j_m \, ds,$$

for all $v_i \in V_i$, $v_e \in V_e$ and $j_m \in Q_c$. After defining the corresponding bilinear and linear forms

$$\begin{aligned} a(u, v) &= \sigma_e (\nabla u_e, \nabla v_e)_{\Omega_e} + \sigma_i (\nabla u_i, \nabla v_i)_{\Omega_i}, \\ b(v, I) &= (v_i - v_e, I)_{\Gamma}, \quad c(I, j) = (I, j)_{\Gamma}, \quad l(j) = (g, j)_{\Gamma}, \end{aligned}$$

and the associated total bilinear form

$$(4.23) \quad A(u, I; v, j) = a(u, v) + b(u, j) + b(v, I) - \frac{\Delta t}{C_m} c(I, j),$$

we can write the problem in the form of a penalized saddle point problem [10]: find $(u, I_m) \in V \times Q_c$ such that

$$(4.24) \quad A(u, I_m; v, j_m) = l(j_m)$$

for all $(v, j_m) \in V \times Q_c$.

Next, we show that problem (4.24) is well-posed. To analyze its well-posedness, we introduce the following norms on the spaces V and Q_c ,

$$(4.25) \quad \|u\|_V^2 = \sigma_e \|\nabla u_e\|_{\Omega_e}^2 + \sigma_i \|\nabla u_i\|_{\Omega_i}^2 + \|u_i - u_e\|_{\Gamma}^2,$$

$$(4.26) \quad \|j_m\|_Q^2 = \|j_m\|_{-1/2, \Gamma}^2,$$

$$(4.27) \quad \|j_m\|_{Q_c}^2 = \|j_m\|_{\Gamma}^2,$$

$$(4.28) \quad \|(v, j_m)\|^2 = \|v\|_V^2 + \|j_m\|_Q^2 + \frac{\Delta t}{C_m} \|j_m\|_{Q_c}^2.$$

The following lemma then shows that the weak formulation (4.24) indeed satisfies an inf-sup condition.

LEMMA 4.1. *For $0 \leq \frac{\Delta t}{C_m} \leq 1$ and $g \in L^2(\Gamma)$ the saddle point formulation (4.24) is inf-sup stable, i.e., there exists a $\gamma > 0$ such that*

$$\inf_{(u, I_m) \in V \times Q_c} \sup_{(v, j_m) \in V \times Q_c} \frac{A(u, I_m; v, j_m)}{\|(u, I_m)\| \cdot \|(v, j_m)\|} \geq \gamma.$$

Proof. Well-posedness for penalized saddle point problems is discussed in [10]. More specifically, if the problem without the penalization term satisfies the LBB conditions, meaning that if the unpenalized problem is well-posed, the penalized problem is stable if in addition the following requirement is satisfied [10, Lemma 3],

$$(4.29) \quad \frac{a(u, u)}{\|u\|_V} + \sup_{I_m \in Q_c} \frac{b(u, I_m)}{\|I_m\|_Q + \varepsilon \|I_m\|_{Q_c}} \geq \alpha \|u\|_V \quad \forall u \in V,$$

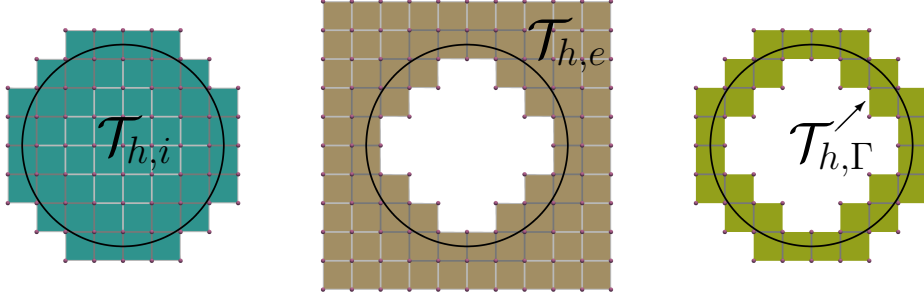


Fig. 4.2: Illustration of the computational domains for the multi-dimensional discretization with the (left) intracellular, (middle) extracellular and (right) interface computational domains.

for some $\alpha > 0$, where $\varepsilon = \sqrt{\frac{\Delta t}{C_m}}$ need to satisfy $0 \leq \varepsilon \leq 1$. The unpenalized version of (4.24) is shown to be well-posed in [37]. It remains to show that (4.29) holds. We start by noting that we have a Gelfand triple with continuous embeddings $H^{\frac{1}{2}}(\Gamma) \subset L^2(\Gamma) \subset H^{-\frac{1}{2}}(\Gamma)$ and that the jump $u_i|_{\Gamma} - u_e|_{\Gamma}$ of a function $u \in V$ is in $H^{\frac{1}{2}}(\Gamma)$. This implies that $\|u_i - u_e\|_Q \leq C_1 \|u_i - u_e\|_{Q_c} \leq C_2 \|u_i - u_e\|_{1/2, \Gamma}$ for some positive constants C_1, C_2 , and thus we conclude that

$$(4.30) \quad \frac{a(u, u)}{\|u\|_V} + \sup_{I_m \in Q_c} \frac{b(u, I_m)}{\|I_m\|_Q + \varepsilon \|I_m\|_{Q_c}}$$

$$(4.31) \quad \geq \frac{\sigma_e \|\nabla u_e\|_{\Omega_e}^2 + \sigma_i \|\nabla u_i\|_{\Omega_i}^2}{\|u\|_V} + \frac{b(u, u_i|_{\Gamma} - u_e|_{\Gamma})}{\|u_i - u_e\|_Q + \varepsilon \|u_i - u_e\|_{Q_c}}$$

$$(4.32) \quad \geq \frac{\sigma_e \|\nabla u_e\|_{\Omega_e}^2 + \sigma_i \|\nabla u_i\|_{\Omega_i}^2}{\|u\|_V} + \frac{\|u_i - u_e\|_{\Gamma}^2}{C \|u_i - u_e\|_{\Gamma}} \geq \alpha \|u\|_V. \quad \square$$

4.2.1. Cut finite element formulation. Next, we devise a CutFEM formulation for the multi-dimensional primal formulation. As for the single-dimensional problem, the two active background meshes $\mathcal{T}_{h,i}$ and $\mathcal{T}_{h,e}$ are used to define approximation spaces for the intra and extra-cellular potentials (see Figure 4.2). To discretize the surface-bounded current I_m , we now also define an active mesh associated with the membrane surface,

$$(4.33) \quad \mathcal{T}_{h,\Gamma} = \{T \in \tilde{\mathcal{T}}_h \mid T \cap \Gamma \neq \emptyset\},$$

and the corresponding set of interior faces,

$$\mathcal{F}_{h,\Gamma} = \{F = T^+ \cap T^- \mid T^+, T^- \in \mathcal{T}_{h,\Gamma} \text{ and } T^+ \neq T^-\}.$$

As finite element spaces, we employ first-order continuous piecewise linear elements for the potentials and constant linear elements for the current,

$$V_{h,i} = \mathbb{P}_c^1(\mathcal{T}_{h,i}), \quad V_{h,e} = \{v \in \mathbb{P}_c^1(\mathcal{T}_{h,e}) : v|_{\partial\Omega} = 0\}, \quad Q_h = \mathbb{P}_{dc}^0(\mathcal{T}_{h,\Gamma}),$$

and as before, we set $V_h = V_{h,i} \times V_{h,e}$. We emphasize that the finite element space for the current is defined on the active background mesh $\mathcal{T}_{h,\Gamma}$ and not on Γ only.

A preliminary and unstabilized unfitted multi-dimensional finite element formulation of the EMI PDEs would be: find $(u_h, I_{m,h}) \in V_h \times Q_h$ such that

$$(4.34a) \quad a(u_h, v_h) + b(v_h, I_{m,h}) = 0, \quad \forall v_h \in V_h,$$

$$(4.34b) \quad b(u_h, j_{m,h}) - \frac{\Delta t}{C_m} c(I_{m,h}, j_{m,h}) = l(j_{m,h}), \quad \forall j_{m,h} \in Q_h,$$

with total bilinear form

$$A(u_h, I_h; v_h, j_h) = a(u_h, v_h) + b(v_h, I_h) + b(u_h, j_h) - \frac{\Delta t}{C_m} c(I_h, j_h).$$

In order to render this discretization scheme both stable and geometrically robust, we will add two stabilization terms. First, as for the single-dimensional formulation, we add the ghost penalty g_h defined in (4.14) to ensure that the presence of small cut elements does not lead to solely negligible contributions to total bilinear form a . Otherwise, the condition number of the system matrix would be highly dependent on the particular cut configuration. Second, in the spirit of [14, 12], we define a stabilization operator

$$s_h(I_h, j_h) = \phi \sum_{F \in \mathcal{F}_{h,\Gamma}} ([I_h], [j_h])_F,$$

where

$$\phi = \max \left\{ \frac{\Delta t}{C_m}, h \right\},$$

which ensures that the unperturbed saddle point problem with $\Delta t = 0$ satisfies an inf-sup condition.

This results in the stabilized bilinear form,

$$(4.35) \quad A_h(u_h, I_h; v_h, j_h) = A(u_h, I_h; v_h, j_h) + g_h(u_h, v_h) - s_h(I_h, j_h),$$

and final stabilized CutFEM discretization for the multi-dimensional primal formulation: find $(u_h, I_{m,h}) \in V_h \times Q_h$ such that

$$(4.36) \quad A_h(u_h, I_{m,h}; v_h, j_{m,h}) = l(j_{m,h})$$

for all $(v_h, j_{m,h}) \in V_h \times Q_h$.

5. Unfitted discretizations of the interface ODE step. When solving the EMI model on a fitted mesh, the ODE-system is naturally solved on each of the interface mesh vertices, degrees of freedom or quadrature points [51]. For an unfitted mesh, there are no longer any mesh points on the interface. To overcome this problem, we here introduce a new unfitted discretization of ODEs based on a stabilized mass matrix approach, similar to a finite element discretization in time of parabolic PDEs.

We begin by introducing a weak formulation based on a stabilized L^2 -projection problem on the surface. Let $f \in L^2(\Gamma)$ be a given function on the surface Γ . For the multi-dimensional formulation, we defined the active mesh associated with the cells that are cut by Γ as $\mathcal{T}_{h,\Gamma}$. Now we use $\mathcal{T}_{h,\Gamma}$ to introduce the discrete function space $Q_{h,\text{ode}} = \mathbb{P}_c^1(\mathcal{T}_{h,\Gamma})$ to be the space of piecewise (bi-)linear continuous functions

on $\mathcal{T}_{h,\Gamma}$. The simple and natural way to define the L^2 -projection of f would be: find $u_h \in Q_{h,\text{ode}}$ such that

$$(5.1) \quad m_h(u_h, w) = (f, w)_\Gamma \quad \forall w \in Q_{h,\text{ode}},$$

where $m_h(u_h, w) = (u_h, w)_\Gamma$. However, the discrete formulation (5.1) suffers from similar issues arising in other unstabilized unfitted formulations. In particular, the mass matrix associated with the problem has potentially large condition numbers which in addition are highly dependent on how the background mesh and the membrane surface intersect.

To remedy this problem, several different stabilization operators s_h can be added [17]. The resulting stabilized L^2 -projection is given by: find $u_h \in V_h$ such that

$$(5.2) \quad M_h(u_h, v) \equiv (u_h, v)_\Gamma + s_h(u, v) = (f, v)_\Gamma \quad \forall v \in V_h.$$

In this work, we consider two realizations of $s_h(\cdot, \cdot)$: a face-based stabilization,

$$(5.3) \quad s_h^1(v, w) = \sum_{F \in \mathcal{F}_{\Gamma, h}} \gamma_b h_F^2 ([\partial_n v], [\partial_n w])_F,$$

and a volume normal gradient stabilization

$$(5.4) \quad s_h^2(v, w) = \gamma_b h_F ([\partial_{n_\Gamma} v], [\partial_{n_\Gamma} w])_{\mathcal{T}_{h,\Gamma}},$$

both proposed in [17], where γ_b is some positive parameter. Note that (5.3) resembles the stabilization used for the PDE in the previous section. Importantly, note that s_h^1 is only suitable for first-order elements. The second stabilization can be used for higher-order elements but is harder to implement if the normal-field of Γ is not given naturally on a volume mesh.

Now, we can use the stabilized L^2 -projection to solve the ODE system on an unfitted surface. A weak formulation is obtained by multiplying the time discretized ODEs (3.1) by test functions $w_1, w_2 \in \mathcal{T}_{h,\Gamma}$, yielding

$$(5.5) \quad (v^{n+1} - v^n, w_1)_\Gamma = -\Delta t (I_{\text{ion}}(v^n, s^n), w_1)_\Gamma,$$

$$(5.6) \quad (s^{n+1} - s^n, w_2)_\Gamma = \Delta t (F(v^n, s^n), w_2)_\Gamma.$$

Adding the same stabilization as for the L^2 -projection problem, we arrive at the following system of equations to be solved for each time step $n = 1, \dots, N$,

$$(5.7) \quad M_h(v^{n+1}, w_1) = m_h(v^n - \Delta t I_{\text{ion}}(v^n, s^n), w_1),$$

$$(5.8) \quad M_h(s^{n+1}, w_2) = m_h(s^n + \Delta t F(v^n, s^n), w_2).$$

The initial conditions v^0 and s^0 also needs to be specified. The natural approach is to use the stabilized L^2 -projection of the initial value such that

$$(5.9) \quad M_h(v^0, w_1) = \Delta t m_h(v(t_0)),$$

$$(5.10) \quad M_h(s^0, w_2) = \Delta t m_h(s(t_0)).$$

In our numerical experiments we will have the initial conditions given as explicit expressions, and we will therefore rather use interpolation to define the initial value.

6. Numerical results. We here present numerical experiments using the methods introduced to discretize the EMI model. First, we evaluate the convergence order and geometrical robustness for the PDE- and ODE-steps separately. Next, we perform a convergence study for the full EMI model with an analytical solution. Finally, we run simulations with the coupled EMI Hodgkin-Huxley model.

6.1. Implementation. All numerical experiments have been implemented in the Julia-based [9] finite element framework Gridap [4, 53]. Gridap includes a high-level domain-specific interface in which the weak formulations can be written in near mathematical notation. The plugin GridapEmbedded [54] allows for the use of unfitted meshes, with the boundary of the physical domain defined as a level set function. In addition, the package STLCutters [41] has been used to instead represent the boundary as an STL surface. In all experiments, we set the penalty parameter for both the PDE-step and ODE-step $\gamma = \gamma_b = 0.1$.

6.2. Multi-dimensional CutFEM discretization converges at optimal order. We consider a convergence study for the multi-dimensional CutFEM discretization of problem (3.2). For numerical studies concerning the single-dimensional formulation, we refer to [33, 40]. We use the method of manufactured solutions, and include additional source terms f_i, f_e on the right-hand sides of the first two equations, respectively, in (3.2) and consider the potentially non-homogeneous boundary condition $u = u_{bc}$ on $\partial\Omega$. Generally, we define the intracellular domain based on a level set function φ , and the extracellular to be the remaining part of the total domain.

$$(6.1) \quad \Omega_i = \{(x, y) \in \mathbb{R}^2 \mid \varphi(x, y) < 0\}, \quad \Omega_e = \Omega \setminus \Omega_i.$$

To begin, we define a total domain by $\Omega_1 = [-1.8, 1.8] \times [-2.05, 1.55]$, and let the level set function be given by

$$(6.2) \quad \varphi_1(x, y) = x^2 + y^2 + y \sin((x+1)^2) - 1.5.$$

We construct a manufactured solution by setting

$$(6.3) \quad u_i(x, y) = \frac{1}{\sigma_i} \sin(0.5\pi x) \cos(0.5\pi y),$$

$$(6.4) \quad u_e(x, y) = \frac{1}{\sigma_e} \sin(0.5\pi x) \cos(0.5\pi y),$$

$$(6.5) \quad I_m(x, y) = \nabla(\sin(0.5\pi x) \cos(0.5\pi y)) \cdot \mathbf{n}_e,$$

where \mathbf{n}_e is the inward normal of Ω_i , and set $\Delta t = 0.2, C_m = 1, \sigma_i = 1.5, \sigma_e = 1$. The problem is solved on a uniform mesh consisting of N^2 uniform square elements, for which we gradually decrease the element size h by setting $N = 2^{2+n}$, with $n = 2, \dots, 6$. For each mesh refinement level n , the error E_n between the analytical solution u and the numerical solution u_n is calculated in a chosen norm (to be further specified),

$$E_n = \|u - u_n\| = \|e_u\|,$$

and the experimental order of convergence (EOC) is calculated via

$$\text{EOC} = \frac{\log(E_{n-1}/E_n)}{\log(h_{n-1}/h_n)}.$$

Table 2: Error and convergence rates for the CutFEM multi-dimensional formulation in the spatial convergence study.

N	$\ e_u\ _{\Omega_1 \cup \Omega_2}$	EOC	$ e_u _{1, \Omega_1 \cup \Omega_2}$	EOC	$\ e_{I_m}\ _{\Gamma}$	EOC
16	$3.42 \cdot 10^{-2}$		$4.84 \cdot 10^{-1}$		$4.37 \cdot 10^{-1}$	
32	$8.62 \cdot 10^{-3}$	1.99	$2.32 \cdot 10^{-1}$	1.06	$2.11 \cdot 10^{-1}$	1.05
64	$2.18 \cdot 10^{-3}$	1.98	$1.14 \cdot 10^{-1}$	1.03	$1.01 \cdot 10^{-1}$	1.06
128	$5.34 \cdot 10^{-4}$	2.03	$5.63 \cdot 10^{-2}$	1.02	$4.51 \cdot 10^{-2}$	1.17
256	$1.36 \cdot 10^{-4}$	1.98	$2.81 \cdot 10^{-2}$	1.01	$2.09 \cdot 10^{-2}$	1.11

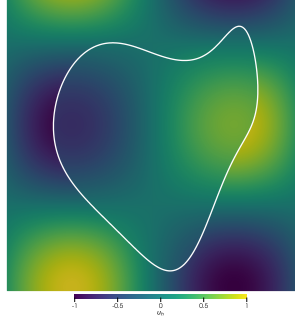


Fig. 6.1: Solution plot for the CutFEM formulations solved on a mesh with 256×256 elements.

The resulting errors and convergence rates are given in Table 2. We see that the convergence rates are optimal, giving first-order convergence in the H^1 -semi-norm and second-order convergence in the L^2 -norm for u . The solution for $N = 256$ is depicted in Figure 6.1.

6.3. CutFEM condition numbers rely on stabilization for robustness.

Next, we perform a sensitivity study to check how different cut configurations affect the condition number of the stiffness matrix related to the problem. The stiffness matrix \mathcal{A} based on the discrete form A_h is defined by the relation

$$(\mathcal{A}V, W)_{\mathbb{R}^N} = A_h(v, w) \quad \forall v, w \in V_h.$$

The condition number of the stiffness matrix is defined by

$$\kappa(\mathcal{A}) = \|\mathcal{A}\|_{\mathbb{R}^N} \|\mathcal{A}^{-1}\|_{\mathbb{R}^N},$$

with the corresponding norm defined by

$$\|\mathcal{A}\|_{\mathbb{R}^N} = \sup_{v \in \mathbb{R}^N \setminus \mathbf{0}} \frac{\|\mathcal{A}V\|_{\mathbb{R}^N}}{\|V\|_{\mathbb{R}^N}}.$$

Here, we compute the condition numbers with the `cond` method provided in Julia, with the 2-norm. By repeatedly moving Ω_i while assembling the stiffness matrices and computing the associated condition number, we evaluate how sensitive the condition number of the different formulations (non-stabilized versus stabilized) is to the configuration of the cut.

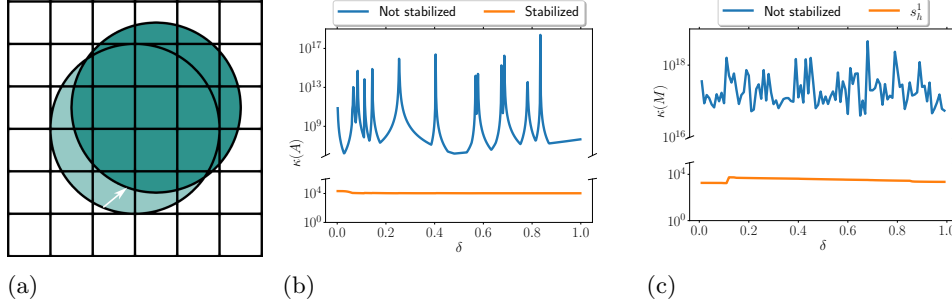


Fig. 6.2: (a) Illustration of how the sensitivity analysis is performed, with the position of the intracellular domain for the first and last iteration. (b-c) The condition numbers of the stiffness matrix for the PDE-step (b) and of the mass matrix for the ODE-step (c) versus the translation parameter δ , without and with two different stabilization formulations. Note that the scaling of the axes is different. For the unstabilized formulation for the ODE-step, $\delta = 0.315$ and $\delta = 0.43$ give singular matrices.

Specifically, let Γ_δ be a circle with radius 0.5, and the center of the circle for step m be defined by

$$(6.6) \quad S = \delta \left(\frac{1}{N}, \frac{1}{N} \right), \quad \delta = \frac{m}{M_\delta},$$

where M_δ is the number of steps, and N is the mesh size. We set $N = 32$, $M_\delta = 500$, $\Delta t = 0.5$, $\sigma_e = 2$, $\sigma_1 = 1$, $C_m = 1$. Figure 6.2(a) shows how the circular interface is moved from the first to the last iteration. The corresponding condition numbers (Figure 6.2 (b)) demonstrate that the non-stabilized formulation is very sensitive to the particular cut configurations, in contrast to the stabilized formulation where the condition numbers are practically constant.

6.4. Geometrical robustness of the unfitted ODE discretization. To examine the geometrical robustness of the unfitted discretization of the ODE steps, we again consider a numerical sensitivity study. We assemble the mass matrix \mathcal{M} associated with (5.2), on different cut configurations and with and without stabilization, and compute the corresponding condition numbers. Specifically, we set $N = 32$, $M_\delta = 100$ and let the stabilization terms be as defined in Section 5. We observe (Figure 6.2 (c)) that the condition numbers for the unstabilized formulation are very high, and even that the projection is singular for some cut configurations. The condition numbers of the s_h^1 formulation are substantially lower, on the order of $10^3 - 10^4$. The condition numbers of the s_h^2 formulation are lower yet again, on the order of $10 - 10^2$.

6.5. Unfitted ODE discretization converges at optimal order. Next, we conduct numerical experiments to test the convergence rates for the discretization of ODEs on the surface alone, using the following linear system of ODEs defined over the membrane surface:

$$v_t = -s \quad s_t = v.$$

We consider a structured background mesh over the domain $\Omega_2 = [-1, 1]^3$ consisting of uniform cubes, where N^3 is the total number of elements. The level set

Table 3: Errors and convergence rates for the unfitted ODE discretization under spatial and temporal refinement.

N/M	$\ e_v\ _{L^\infty L^2(\Gamma)}$	EOC	$\ e_v\ _{L^2 L^2(\Gamma)}$	EOC
8/2	$4.64 \cdot 10^{-1}$		$5.98 \cdot 10^{-1}$	
16/4	$2.14 \cdot 10^{-1}$	1.12	$2.19 \cdot 10^{-1}$	1.45
32/8	$9.01 \cdot 10^{-2}$	1.25	$9.18 \cdot 10^{-2}$	1.25
64/16	$4.46 \cdot 10^{-2}$	1.02	$4.14 \cdot 10^{-2}$	1.15
128/32	$2.43 \cdot 10^{-2}$	0.87	$1.95 \cdot 10^{-2}$	1.08
N/M	$\ e_s\ _{L^\infty L^2(\Gamma)}$	EOC	$\ e_s\ _{L^2 L^2(\Gamma)}$	EOC
8/2	1.07		1.09	
16/4	$5.94 \cdot 10^{-1}$	0.85	$5.15 \cdot 10^{-1}$	1.08
32/8	$2.72 \cdot 10^{-1}$	1.13	$2.27 \cdot 10^{-1}$	1.18
64/16	$1.25 \cdot 10^{-1}$	1.12	$1.05 \cdot 10^{-1}$	1.12
128/32	$5.98 \cdot 10^{-2}$	1.07	$4.99 \cdot 10^{-2}$	1.07

function defining the surface is defined by

$$\varphi_2(x, y, z) = \frac{x^2}{0.8^2} + y^2 + \frac{z^2}{0.9^2} - 0.8^2.$$

Over this domain, we define manufactured solutions as

$$v(x, y, z, t) = (x^2 + y^3 + z^2) \cos(t), \quad s(x, y, z, t) = (x^2 + y^3 + z^2) \sin(t).$$

The system is solved on the time interval $[0, 2]$ with the number of uniform time intervals set to $M = 2^{n+1}$ with $n = 0, \dots, 4$ and $N = 4M$. For ease of implementation, we utilize the s_h^1 -stabilization here and in the remainder of the manuscript. To evaluate the discretization properties, we let the discrete $L^\infty L^2$ - and (square) $L^2 L^2$ -norms be defined by

$$\|v\|_{L^\infty L^2(\Gamma)} = \max_{m \in [1, \dots, M]} \|v(\cdot, t_m)\|_\Gamma, \quad \|v\|_{L^2 L^2(\Gamma)}^2 = \frac{1}{M} \sum_{m=1}^M \|v(\cdot, t_m)\|_\Gamma^2$$

By evaluating the errors for the series of meshes and time step sizes and estimating the errors of convergence (Table 3), we observe that the discretization errors decay at first-order, as expected.

6.6. Convergence analysis of the unfitted coupled EMI discretization.

Next, we perform a series of numerical experiments to validate the whole splitting scheme, where we solve the full EMI system (2.1) augmented by right-hand-sides f_i, f_e in (2.1a) and (2.1b), respectively, and a simplified ODE model with given P_1, P_2 :

$$(6.7) \quad v_t = \frac{1}{C_m} (I_m - P_1 + s), \quad s_t = v + P_2.$$

We consider the geometrical configuration as in Section 6.5. We design the manufactured solution,

$$\begin{aligned} u_i &= \frac{1}{\sigma_i} \sin(\pi x) \cos(\pi y) \exp(0.5z) \exp(-0.5t), \\ u_e &= \frac{1}{\sigma_e} \sin(\pi x) \cos(\pi y) \exp(0.5z) \exp(-0.5t), \\ s &= I_m, \end{aligned}$$

and again refine both the spatial and temporal resolution with $M = [4, 6, 8, 12, 16]$ and $N = 4M$. To measure the errors, we employ the discrete $L^\infty X$ - and square $L^2 X$ -norms defined by

$$\|u\|_{L^\infty X(\Omega)} = \max_{m \in [0, \dots, M]} \|u(\cdot, t_m)\|_{X, \Omega}, \quad \|u\|_{L^2 X(\Omega)}^2 = \frac{1}{M} \sum_{m=0}^M \|u(\cdot, t_m)\|_{X, \Omega}^2,$$

where X is either the L^2 - or the H^1 - norm. Norms and rates of convergence are listed in Table 4 for the single-dimensional formulation, and in Table 5 for the multi-dimensional formulation. We observe first-order convergence for u , v , s and I_m in all relevant norms, which is as expected in light of the first-order splitting scheme.

6.7. Neuronal action potentials and local field potential on unfitted geometries. We finally consider simulating the neuronal potential and the surrounding extracellular potential (local field potential) triggered by a sufficiently large stimulus. The neuron-ECS interface is defined by a specific neuronal reconstruction¹ meshed to an STL format [44]. We define Ω_i by the interior of this reconstructed surface, and Ω by its bounding-box extended by $\pm 8\mu\text{m}$ in each direction. As usual, $\Omega_e = \Omega \setminus \Omega_i$. We use the Hodgkin-Huxley membrane model as described in Section 2, and set all parameters as defined in Table 1. To induce an action potential, we apply a stimulus in the time interval $[0, 0.5]$ in an upper part of the neuron (the part of the membrane which is inside the domain $D = \{(x, y, z) \in \Omega_i : y > 100\mu\text{m}\}$), illustrated in figure Figure 6.3. We consider the multi-dimensional formulation of the PDE step, and the s_h^1 -stabilization of the ODE formulation, and divide the domain into square elements ($108 \times 146 \times 36$).

The resulting approximations for the membrane, intra and extracellular potentials in three points located close to each other are shown in Figure 6.3, together with snapshots of the membrane and extracellular potentials. We observe that the cell is depolarized before it is repolarized.

To study the numerical convergence of the membrane and cellular potential approximations on the unfitted geometry, we also run a series of spatial refinements ($54 \times 73 \times 18$, $78 \times 106 \times 26$, and $108 \times 146 \times 36$) on the time interval $[0, 1.5\text{ms}]$, with $\Delta t = 0.01\text{ms}$. Comparing the membrane and extracellular potentials from the same points as before (Figure 6.3), we observe that the solutions seem to converge.

7. Conclusions and outlook. We proposed a new CutFEM framework to discretize the EMI problem on geometrically resolved cell-by-cell models. Extensive numerical studies showed that our framework gives the same convergence rates as expected from a standard fitted finite element discretization and that it is insensitive to how the embedded cell geometry cuts the background mesh ensuring the geometrical

¹Data set with ID NMO_76781 [34] from neuromorpho.org[2].

Table 4: Errors and convergence rates under spatial and temporal refinement with the single-dimensional formulation.

N/M	$\ e_u\ _{L^\infty L^2(\Omega)}$	EOC	$\ e_u\ _{L^\infty H^1(\Omega)}$	EOC	$\ e_v\ _{L^\infty L^2(\Gamma)}$	EOC	$\ e_s\ _{L^\infty L^2(\Gamma)}$	EOC
16/4	$2.94 \cdot 10^{-2}$		$4.13 \cdot 10^{-1}$		$7.84 \cdot 10^{-2}$		$2.51 \cdot 10^{-1}$	
24/6	$1.89 \cdot 10^{-2}$	1.09	$2.87 \cdot 10^{-1}$	0.90	$5.55 \cdot 10^{-2}$	0.85	$1.45 \cdot 10^{-1}$	1.36
32/8	$1.40 \cdot 10^{-2}$	1.05	$2.20 \cdot 10^{-1}$	0.92	$4.30 \cdot 10^{-2}$	0.89	$9.94 \cdot 10^{-2}$	1.30
48/12	$9.28 \cdot 10^{-3}$	1.01	$1.50 \cdot 10^{-1}$	0.95	$2.98 \cdot 10^{-2}$	0.90	$6.08 \cdot 10^{-2}$	1.21
64/16	$6.96 \cdot 10^{-3}$	1.00	$1.14 \cdot 10^{-1}$	0.96	$2.28 \cdot 10^{-2}$	0.94	$4.36 \cdot 10^{-2}$	1.15
N/M	$\ e_u\ _{L^2 L^2(\Omega)}$	EOC	$\ e_u\ _{L^2 H^1(\Omega)}$	EOC	$\ e_v\ _{L^2 L^2(\Gamma)}$	EOC	$\ e_s\ _{L^2 L^2(\Gamma)}$	EOC
16/4	$2.75 \cdot 10^{-2}$		$3.55 \cdot 10^{-1}$		$6.98 \cdot 10^{-2}$		$2.13 \cdot 10^{-1}$	
24/6	$1.69 \cdot 10^{-2}$	1.20	$2.44 \cdot 10^{-1}$	0.93	$4.82 \cdot 10^{-2}$	0.91	$1.13 \cdot 10^{-1}$	1.57
32/8	$1.23 \cdot 10^{-2}$	1.11	$1.86 \cdot 10^{-1}$	0.94	$3.71 \cdot 10^{-2}$	0.91	$7.29 \cdot 10^{-2}$	1.51
48/12	$7.98 \cdot 10^{-3}$	1.07	$1.26 \cdot 10^{-1}$	0.96	$2.54 \cdot 10^{-2}$	0.94	$4.15 \cdot 10^{-2}$	1.39
64/16	$5.92 \cdot 10^{-3}$	1.04	$9.50 \cdot 10^{-2}$	0.97	$1.93 \cdot 10^{-2}$	0.95	$2.86 \cdot 10^{-2}$	1.30

Table 5: Errors and convergence rates under spatial and temporal refinement with the multi-dimensional formulation.

N/M	$\ e_u\ _{L^\infty L^2(\Omega)}$	EOC	$\ e_u\ _{L^\infty H^1(\Omega)}$	EOC	$\ e_v\ _{L^\infty L^2(\Gamma)}$	EOC	$\ e_s\ _{L^\infty L^2(\Gamma)}$	EOC	$\ e_{I_m}\ _{L^\infty L^2(\Gamma)}$	EOC
16/4	$2.64 \cdot 10^{-2}$		$4.20 \cdot 10^{-1}$		$8.66 \cdot 10^{-2}$		$2.36 \cdot 10^{-1}$		$4.46 \cdot 10^{-1}$	
24/6	$1.92 \cdot 10^{-2}$	0.79	$2.90 \cdot 10^{-1}$	0.91	$6.35 \cdot 10^{-2}$	0.76	$1.08 \cdot 10^{-1}$	1.93	$3.07 \cdot 10^{-1}$	0.92
32/8	$1.30 \cdot 10^{-2}$	1.37	$2.22 \cdot 10^{-1}$	0.94	$4.39 \cdot 10^{-2}$	1.29	$8.08 \cdot 10^{-2}$	1.00	$2.37 \cdot 10^{-1}$	0.91
48/12	$8.48 \cdot 10^{-3}$	1.04	$1.50 \cdot 10^{-1}$	0.95	$2.92 \cdot 10^{-2}$	1.01	$4.85 \cdot 10^{-2}$	1.26	$1.60 \cdot 10^{-1}$	0.97
64/16	$6.23 \cdot 10^{-3}$	1.07	$1.14 \cdot 10^{-1}$	0.97	$2.16 \cdot 10^{-2}$	1.05	$3.35 \cdot 10^{-2}$	1.28	$1.19 \cdot 10^{-1}$	1.01
N/M	$\ e_u\ _{L^2 L^2(\Omega)}$	EOC	$\ e_u\ _{L^2 H^1(\Omega)}$	EOC	$\ e_v\ _{L^2 L^2(\Gamma)}$	EOC	$\ e_s\ _{L^2 L^2(\Gamma)}$	EOC	$\ e_{I_m}\ _{L^2 L^2(\Gamma)}$	EOC
16/4	$2.50 \cdot 10^{-2}$		$3.70 \cdot 10^{-1}$		$7.81 \cdot 10^{-2}$		$2.03 \cdot 10^{-1}$		$4.23 \cdot 10^{-1}$	
24/6	$1.73 \cdot 10^{-2}$	0.90	$2.52 \cdot 10^{-1}$	0.95	$5.59 \cdot 10^{-2}$	0.82	$9.18 \cdot 10^{-2}$	1.96	$2.87 \cdot 10^{-1}$	0.96
32/8	$1.15 \cdot 10^{-2}$	1.43	$1.89 \cdot 10^{-1}$	0.99	$3.83 \cdot 10^{-2}$	1.32	$7.20 \cdot 10^{-2}$	0.84	$2.16 \cdot 10^{-1}$	0.99
48/12	$7.36 \cdot 10^{-3}$	1.10	$1.27 \cdot 10^{-1}$	0.98	$2.52 \cdot 10^{-2}$	1.03	$4.07 \cdot 10^{-2}$	1.41	$1.45 \cdot 10^{-1}$	0.98
64/16	$5.34 \cdot 10^{-3}$	1.11	$9.58 \cdot 10^{-2}$	0.99	$1.85 \cdot 10^{-2}$	1.07	$2.63 \cdot 10^{-2}$	1.52	$1.08 \cdot 10^{-1}$	1.03

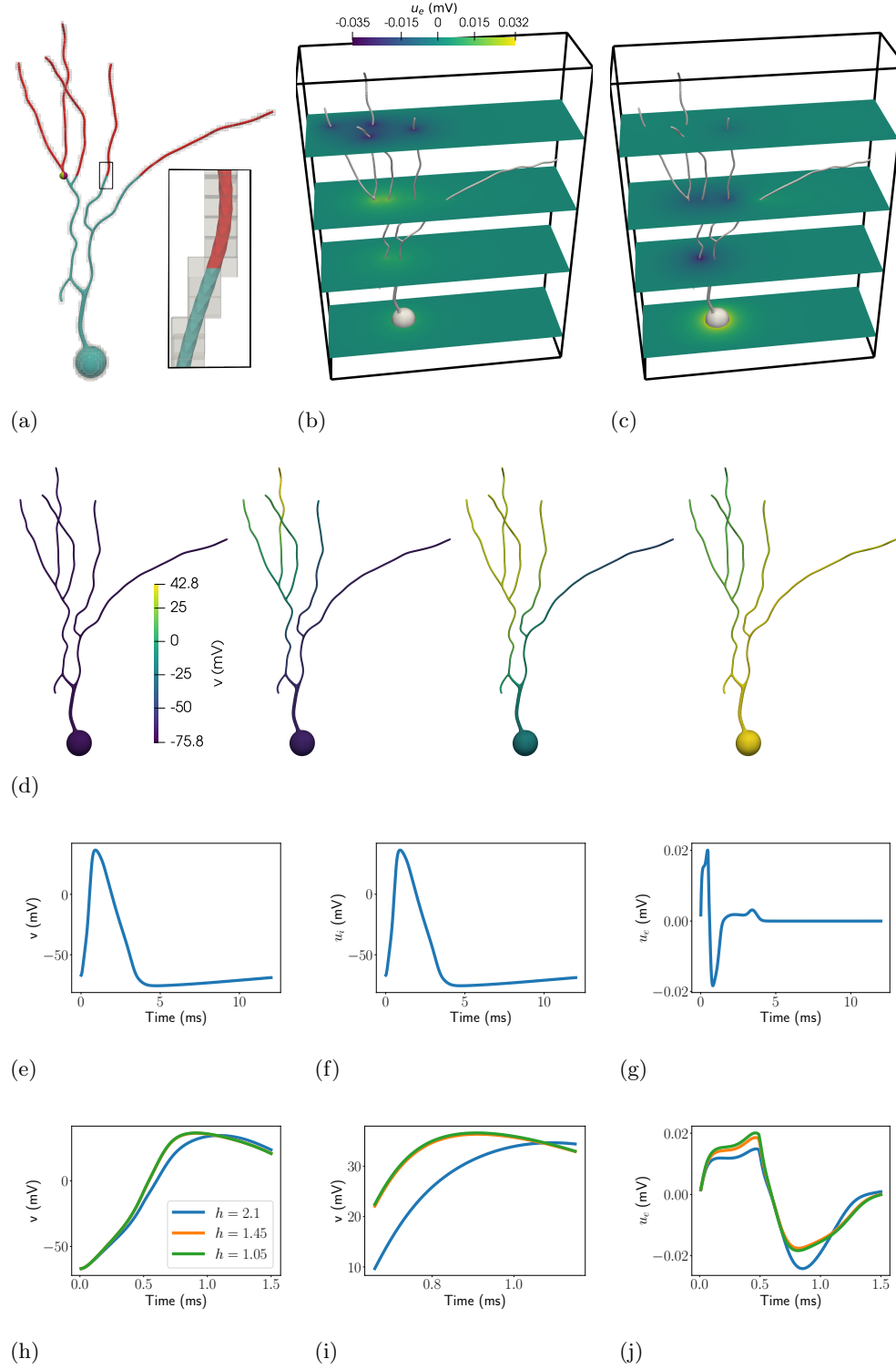


Fig. 6.3: (a) The intracellular domain and its active mesh, showing stimulated parts of dendrites. (b–c) Simulated extracellular potential at $t = 0.5$ ms and $t = 1.1$ ms. (d) Membrane potential at $t = 0.0, 0.5, 1.1, 1.5$ ms. (e–g) Traces of the membrane (e), intracellular (f) and extracellular (g) potential over time, evaluated at close points shown in (a). (h–j) Traces of the neuronal membrane potential (i) and (j, zoom) and extracellular potential (h) for different spatial resolutions.

robustness of our method. The CutFEM framework for the EMI model circumvents the time-consuming generation of high-quality unstructured 3D volume meshes required for accurate standard FEM based computations. To obtain a more holistic simulation pipeline, a next natural step would be to implement a user-friendly interface which allows to feed imaging data of the neuron cells directly into the numerical solver.

In this work, we focused on two CutFEM discretizations of the EMI PDE step both of which were based on a primal formulation of the potential equations in the extra- and intracellular domains. Based on the idea of $H(\text{div})$ -conforming formulation of the EMI problem as suggested in, e.g., [36], it will be also interesting to explore the advantages and disadvantages of emerging $H(\text{div})$ -conforming CutFEM formulations [38, 27] in the context of geometrically resolved cell-by-cell discretizations.

Solving the EMI model is computationally demanding due to the multiple scales in space and time characteristic for each subsystem. Moreover, the linear system arising from the decoupled PDE requires solving a large linear system. To be able to apply the CutFEM framework to large-scale problems and realistic representation of neural cell networks, we need to look into the possibilities for parallelization. This will require the design and implementation of efficient and parallelizable mesh intersecting algorithms, and many of the arising challenges have been addressed in the work [35]. Looking into preconditioning to improve robustness and scalability would also be beneficial. Since the problem is coupled across dimensions, this requires tailored methods, and for the fitted EMI problem the design of algebraic multigrid methods has been considered in the very recent preprint [11]. Moreover, to prevent unphysical communication between dendrites through the extracellular space caused by a too low resolution in the background mesh, we also suggest combining our approach with adaptive mesh refinement based on octrees [18]. Finally, it might be worthwhile to consider extending the first-order Godunov splitting scheme to a second-order Strang splitting to improve computationally efficiency.

Acknowledgments. We graciously acknowledge useful discussions and support from Miroslav Kuchta in connection with the neuronal geometry.

REFERENCES

- [1] A. AGUDELO-TORO AND A. NEEF, *Computationally efficient simulation of electrical activity at cell membranes interacting with self-generated and externally imposed electric fields*, Journal of Neural Engineering, 10 (2013), p. 026019, <https://doi.org/10.1088/1741-2560/10/2/026019>.
- [2] G. A. ASCOLI, D. E. DONOHUE, AND M. HALAVI, *NeuroMorpho.Org: A Central Resource for Neuronal Morphologies*, The Journal of Neuroscience, 27 (2007), pp. 9247–9251, <https://doi.org/10.1523/JNEUROSCI.2055-07.2007>.
- [3] N. M. ATALLAH, C. CANUTO, AND G. SCOVAZZI, *The shifted boundary method for solid mechanics*, International Journal for Numerical Methods in Engineering, 122 (2021), pp. 5935–5970, <https://doi.org/10/gk49t8>, <https://onlinelibrary.wiley.com/doi/abs/10.1002/nme.6779> (accessed 2023-05-19).
- [4] S. BADIA AND F. VERDUGO, *Gridap: An extensible Finite Element toolbox in Julia*, Journal of Open Source Software, 5 (2020), p. 2520, <https://doi.org/10.21105/joss.02520>.
- [5] S. BADIA, F. VERDUGO, AND A. F. MARTÍN, *The aggregated unfitted finite element method for elliptic problems*, Comput. Methods Appl. Mech. Engrg., 336 (2018), pp. 533–553, <https://doi.org/10.1016/j.cma.2018.03.022>.
- [6] P. BASTIAN AND C. ENGWER, *An unfitted finite element method using discontinuous Galerkin*, International Journal for Numerical Methods in Engineering, 79 (2009), pp. 1557–1576, <https://doi.org/10.1002/nme.2631>.
- [7] F. BEN BELGACEM, C. BERNARDI, F. JELASSI, AND M. MINT BRAHIM, *Finite Element Methods*

- for the Temperature in Composite Media with Contact Resistance, *Journal of Scientific Computing*, 63 (2015), pp. 478–501, <https://doi.org/10.1007/s10915-014-9907-0>.
- [8] N. BERRE, *Supplementary material (Code) for Cut finite element discretizations of cell-by-cell EMI electrophysiology models*, June 2023, <https://doi.org/10.5281/zenodo.8068506>, <https://doi.org/10.5281/zenodo.8068506>.
 - [9] J. BEZANSON, A. EDELMAN, S. KARPINSKI, AND V. B. SHAH, *Julia: A Fresh Approach to Numerical Computing*, *SIAM Review*, 59 (2017), pp. 65–98, <https://doi.org/10.1137/141000671>.
 - [10] D. BRAESS, *Stability of saddle point problems with penalty*, *ESAIM: Mathematical Modelling and Numerical Analysis*, 30 (1996), pp. 731–742, <https://doi.org/10.1051/m2an/1996300607311>.
 - [11] A. BUDISA, X. HU, M. KUČTA, K.-A. MARDAL, AND L. T. ZIKATANOV, *Algebraic multigrid methods for metric-perturbed coupled problems*, May 2023, <https://arxiv.org/abs/2305.06073>.
 - [12] E. BURMAN, *Projection stabilization of Lagrange multipliers for the imposition of constraints on interfaces and boundaries*, *Numerical Methods for Partial Differential Equations*, 30 (2014), pp. 567–592, <https://doi.org/10.1002/num.21829>.
 - [13] E. BURMAN, S. CLAUS, P. HANSBO, M. G. LARSON, AND A. MASSING, *CutFEM: Discretizing geometry and partial differential equations*, *International Journal for Numerical Methods in Engineering*, 104 (2015), pp. 472–501, <https://doi.org/10.1002/nme.4823>.
 - [14] E. BURMAN AND P. HANSBO, *Interior-penalty-stabilized Lagrange multiplier methods for the finite-element solution of elliptic interface problems*, *IMA J. Numer. Anal.*, 30 (2009), pp. 870–885, <https://doi.org/10.1093/imanum/drn081>.
 - [15] E. BURMAN AND P. HANSBO, *Fictitious domain finite element methods using cut elements: II. A stabilized Nitsche method*, *Applied Numerical Mathematics*, 62 (2012), pp. 328–341, <https://doi.org/10.1016/j.apnum.2011.01.008>.
 - [16] E. BURMAN, P. HANSBO, M. G. LARSON, AND A. MASSING, *Cut finite element methods for partial differential equations on embedded manifolds of arbitrary codimensions*, *ESAIM: Math. Model. Numer. Anal.*, 52 (2018), pp. 2247–2282, <https://doi.org/10.gh8jr6>.
 - [17] E. BURMAN, P. HANSBO, M. G. LARSON, AND A. MASSING, *Cut finite element methods for partial differential equations on embedded manifolds of arbitrary codimensions*, *ESAIM: Mathematical Modelling and Numerical Analysis*, 52 (2018), pp. 2247–2282, <https://doi.org/10.1051/m2an/2018038>.
 - [18] C. BURSTEDDE, L. C. WILCOX, AND O. GHATTAS, *P4est: Scalable Algorithms for Parallel Adaptive Mesh Refinement on Forests of Octrees*, *SIAM Journal on Scientific Computing*, 33 (2011), pp. 1103–1133.
 - [19] C. CALÌ, M. AGUS, K. KARE, D. J. BOGES, H. LEHVÄSLAIHO, M. HADWIGER, AND P. J. MAGISTRETTI, *3D cellular reconstruction of cortical glia and parenchymal morphometric analysis from Serial Block-Face Electron Microscopy of juvenile rat*, *Progress in Neurobiology*, 183 (2019), p. 101696, <https://doi.org/10.1016/j.pneurobio.2019.101696>.
 - [20] S. CLAUS, P. KERFRIDEN, F. MOSHFEGHIFAR, S. DARKNER, K. ERLEBEN, AND C. WONG, *Contact modeling from images using cut finite element solvers*, *Advanced Modeling and Simulation in Engineering Sciences*, 8 (2021), p. 13, <https://doi.org/10/gkf8x8>, <https://doi.org/10.1186/s40323-021-00197-2> (accessed 2023-05-19).
 - [21] F. DE PRENTER, C. V. VERHOOSSEL, E. H. VAN BRUMMELEN, M. G. LARSON, AND S. BADIA, *Stability and Conditioning of Immersed Finite Element Methods: Analysis and Remedies*, *Arch Computat Methods Eng.* (2023), <https://doi.org/10/gr8q4w>, <https://doi.org/10.1007/s11831-023-09913-0> (accessed 2023-05-18).
 - [22] G. R. DE SOUZA, R. KRAUSE, AND S. PEZZUTO, *Boundary integral formulation of the cell-by-cell model of cardiac electrophysiology*, *arXiv preprint arXiv:2302.05281*, (2023).
 - [23] A. J. ELLINGSRUD, A. SOLBRÅ, G. T. EINEVOLL, G. HALNES, AND M. E. Rognes, *Finite element simulation of ionic electrodiffusion in cellular geometries*, *Frontiers in Neuroinformatics*, 14 (2020), p. 11, <https://doi.org/10.3389/fninf.2020.00011>.
 - [24] T. ERDBRÜGGER, A. WESTHOFF, M. HOELTERSHINKEN, J.-O. RADECKE, Y. BUSCHER-MOEHL, A. BUYX, F. WALLOIS, S. PURSIANEN, J. GROSS, R. LENCER, C. ENGWER, AND C. WOLTERS, *CutFEM Forward Modeling for EEG Source Analysis*, *Tech. Report arXiv:2211.17093*, Nov. 2022, <https://doi.org/10.48550/arXiv.2211.17093>, <https://arxiv.org/abs/2211.17093>.
 - [25] S. FARINA, *Modelling astrocytic metabolism in actual cell morphologies*, 2022.
 - [26] S. FARINA, S. CLAUS, J. S. HALE, A. SKUPIN, AND S. P. BORDAS, *A cut finite element method for spatially resolved energy metabolism models in complex neuro-cell morphologies with minimal remeshing*, *Advanced Modeling and Simulation in Engineering Sciences*, 8 (2021),

- pp. 1–32, <https://doi.org/10.1186/s40323-021-00191-8>.
- [27] T. FRACHON, P. HANSBO, E. NILSSON, AND S. ZAHEDI, *A divergence preserving cut finite element method for Darcy flow*, Apr. 2023, <https://arxiv.org/abs/2205.12023>.
 - [28] C. GÜRKAN AND A. MASSING, *A stabilized cut discontinuous Galerkin framework for elliptic boundary value and interface problems*, *Computer Methods in Applied Mechanics and Engineering*, 348 (2019), pp. 466–499, <https://doi.org/10.1016/j.cma.2018.12.041>.
 - [29] A. L. HODGKIN AND A. F. HUXLEY, *A quantitative description of membrane current and its application to conduction and excitation in nerve*, *The Journal of Physiology*, 117 (1952), pp. 500–544, <https://doi.org/10.1113/jphysiol.1952.sp004764>.
 - [30] K. H. JÆGER, A. G. EDWARDS, A. MCCULLOCH, AND A. TVEITO, *Properties of cardiac conduction in a cell-based computational model*, *PLOS Computational Biology*, 15 (2019), pp. 1–35, <https://doi.org/10.1371/journal.pcbi.1007042>.
 - [31] K. H. JÆGER, K. G. HUSTAD, X. CAI, AND A. TVEITO, *Efficient Numerical Solution of the EMI Model Representing the Extracellular Space (E), Cell Membrane (M) and Intracellular Space (I) of a Collection of Cardiac Cells*, *Frontiers in Physics*, 8 (2021), <https://doi.org/10.3389/fphy.2020.579461>.
 - [32] K. H. JÆGER AND A. TVEITO, *Derivation of a cell-based mathematical model of excitable cells*, in *Modeling Excitable Tissue: The EMI Framework*, A. Tveito, K.-A. Mardal, and M. E. Rognes, eds., vol. 7, Springer International Publishing, Cham, Oct. 2021, ch. 1, pp. 1–13, https://doi.org/10.1007/978-3-030-61157-6_1.
 - [33] H. JI, F. WANG, AND J. CHEN, *Unfitted finite element methods for the heat conduction in composite media with contact resistance: Unfitted Method For Heat Conduction With Interface*, *Numerical Methods for Partial Differential Equations*, 33 (2017), pp. 354–380, <https://doi.org/10.1002/num.22111>.
 - [34] B. C. JONGBLOETS, S. LEMSTRA, R. SCHELLINO, M. H. BROEKHOVEN, J. PARKASH, A. J. C. G. M. HELLEMONS, T. MAO, P. GIACOBINI, H. VAN PRAAG, S. DE MARCHIS, G. M. J. RAMAKERS, AND R. J. PASTERKAMP, *Stage-specific functions of Semaphorin7A during adult hippocampal neurogenesis rely on distinct receptors*, *Nature Communications*, 8 (2017), p. 14666, <https://doi.org/10.1038/ncomms14666>.
 - [35] R. KRAUSE AND P. ZULIAN, *A parallel approach to the variational transfer of discrete fields between arbitrarily distributed unstructured finite element meshes*, *Siam Journal On Scientific Computing*, 38 (2016), pp. C307–C333, <https://doi.org/10.1137/15M1008361>.
 - [36] M. KUCHTA, K.-A. MARDAL, AND M. E. ROGNES, *Solving the EMI equations using finite element methods*, in *Modeling Excitable Tissue: The EMI Framework*, A. Tveito, K.-A. Mardal, and M. E. Rognes, eds., Springer International Publishing, Cham, Oct. 2021, pp. 56–69, https://doi.org/10.1007/978-3-030-61157-6_5.
 - [37] B. P. LAMICHANE AND B. I. WOHLMUTH, *Mortar Finite Elements for Interface Problems*, *Computing*, 72 (2004), <https://doi.org/10.1007/s00607-003-0062-y>.
 - [38] C. LEHRENFELD, T. VAN BEECK, AND I. VOULIS, *Analysis of divergence-preserving unfitted finite element methods for the mixed poisson problem*, 2023, <https://arxiv.org/abs/2306.12722>.
 - [39] R. J. LEVEQUE, *Finite Volume Methods for Hyperbolic Problems*, *Cambridge Texts in Applied Mathematics*, Cambridge University Press, Cambridge, 2002, <https://doi.org/10.1017/CBO9780511791253>.
 - [40] X. LI, X. ZHANG, AND X. ZHOU, *High order interface-penalty finite element methods for elliptic interface problems with Robin jump conditions*, *Computer Methods in Applied Mechanics and Engineering*, 390 (2022), p. 114505, <https://doi.org/10.1016/j.cma.2021.114505>.
 - [41] P. MARTORELL, S. BADIA, AND F. VERDUGO, *STLCutters*. Version 1.6., GitHub, 2023, Available at <https://github.com/gridap/STLCutters.jl/>.
 - [42] A. MASSING, M. G. LARSON, A. LOGG, AND M. E. ROGNES, *A stabilized Nitsche fictitious domain method for the Stokes problem*, 61, pp. 604–628, <https://doi.org/10.1007/s10915-014-9838-9>.
 - [43] Y. MORI AND C. PESKIN, *A numerical method for cellular electrophysiology based on the electrodiffusion equations with internal boundary conditions at membranes*, *Communications in Applied Mathematics and Computational Science*, 4 (2009), pp. 85–134, <https://doi.org/10.2140/camcos.2009.4.85>.
 - [44] K. MÖRSCHER, M. BREIT, AND G. QUEISSER, *Generating Neuron Geometries for Detailed Three-Dimensional Simulations Using AnaMorph*, *Neuroinformatics*, 15 (2017), pp. 247–269, <https://doi.org/10.1007/s12021-017-9329-x>.
 - [45] A. NÜSSING, C. H. WOLTERS, H. BRINCK, AND C. ENGWER, *The Unfitted Discontinuous Galerkin Method for Solving the EEG Forward Problem*, *IEEE Transactions on Biomedical Engineering*, 63 (2016), pp. 2564–2575, <https://doi.org/10/f9k7cf>.
 - [46] E. RANK, M. RUESS, S. KOLLMANNBERGER, D. SCHILLINGER, AND A. DÜSTER, *Geometric*

- modeling, isogeometric analysis and the finite cell method*, Comput. Methods Appl. Mech. Engrg., 249 (2012), pp. 104–115, <https://doi.org/10.1016/j.cma.2012.05.022>.
- [47] D. SCHILLINGER, L. DEDE, M. A. SCOTT, J. A. EVANS, M. J. BORDEN, E. RANK, AND T. J. HUGHES, *An isogeometric design-through-analysis methodology based on adaptive hierarchical refinement of NURBS, immersed boundary methods, and T-spline CAD surfaces*, Comput. Methods Appl. Mech. Engrg., 249 (2012), pp. 116–150, <https://doi.org/10.1016/j.cma.2012.03.017>.
 - [48] D. SCHILLINGER AND M. RUESS, *The finite cell method: A review in the context of higher-order structural analysis of cad and image-based geometric models*, Arch. Comput. Methods Engrg., (2014), pp. 1–65, <https://doi.org/10.1007/s11831-014-9115-y>.
 - [49] B. STINNER AND T. BRETSCHNEIDER, *Mathematical modelling in cell migration: tackling biochemistry in changing geometries*, Biochemical Society Transactions, 48 (2020), pp. 419–428, <https://doi.org/10.1042/BST20190311>.
 - [50] J. SUNDNES, B. F. NIELSEN, K. A. MARDAL, X. CAI, G. T. LINES, AND A. TVEITO, *On the computational complexity of the bidomain and the monodomain models of electrophysiology*, Annals of biomedical engineering, 34 (2006), pp. 1088–1097, <https://doi.org/10.1007/s10439-006-9082-z>.
 - [51] A. TVEITO, K. H. JÆGER, M. KUCHTA, K.-A. MARDAL, AND M. E. ROGNES, *A cell-based framework for numerical modeling of electrical conduction in cardiac tissue*, Frontiers in Physics, 5 (2017), p. 48.
 - [52] A. TVEITO, K. H. JÆGER, G. T. LINES, L. PASZKOWSKI, J. SUNDNES, A. G. EDWARDS, T. MÄKI-MARTTUNEN, G. HALNES, AND G. T. EINEVOLL, *An Evaluation of the Accuracy of Classical Models for Computing the Membrane Potential and Extracellular Potential for Neurons*, Frontiers in Computational Neuroscience, 11 (2017), p. 27, <https://doi.org/10.3389/fncom.2017.00027>.
 - [53] F. VERDUGO AND S. BADIA, *The software design of gridap: A finite element package based on the julia JIT compiler*, Computer Physics Communications, 276 (2022), p. 108341, <https://doi.org/10.1016/j.cpc.2022.108341>, <https://doi.org/10.1016/j.cpc.2022.108341>.
 - [54] F. VERDUGO, E. NEIVA, AND S. BADIA, *GridapEmbedded*. Version 0.8., GitHub, 2023, Available at <https://github.com/gridap/GridapEmbedded.jl>.
 - [55] C. V. VERHOOSSEL, G. J. VAN ZWIETEN, B. VAN RIETBERGEN, AND R. DE BORST, *Image-Based Goal-Oriented Adaptive Isogeometric Analysis with Application to the Micro-Mechanical Modeling of Trabecular Bone*, Comput. Methods Appl. Mech. Engrg., 284 (2015), pp. 138–164, <https://doi.org/10/f63fv9>.